Holographic MIMO Communications with Orbital Angular Momentum and Polarization Multiplexing

Arif Ullah, M. Ali Babar Abbasi, Okan Yurduseven, and Hien Quoc Ngo
Centre for Wireless Innovations (CWI), School of Electronics, Electrical Engineering and Computer Science (EEECS),
Queens University Belfast, United Kingdom (UK), Email: {a.ullah, m.abbasi, o.yurduseven, hien.ngo}@qub.ac.uk.

***Abstract*—Holographic multiple-input multiple-output (HMIMO) has emerged as a promising technology for next-generation wireless communication systems with the capability to intelligently control electromagnetic waves through a nearly continuous aperture, offering unprecedented spatial degrees of freedom. In this paper, we analyze the performance of HMIMO that jointly exploits orbital angular momentum (OAM) and polarization multiplexing using a fully polarized uniform circular array (UCA) to enhance channel capacity and enable highly efficient spatial multiplexing within a compact aperture. We present the theoretical framework for the combined multiplexing scheme that utilizes the Green's function-based polarized channel model and validate the performance of the system through extensive simulations. Furthermore, the OAM modes are approximated through the Green's function and validated using the measurements obtained from a fabricated UCA. The results demonstrate that the proposed approach offers a significant performance gain in terms of system capacity compared to the conventional single-polarized OAM.**

***Index Terms*—EM informed channel, holographic MIMO, multiple polarizations, orbital angular momentum.**

I. INTRODUCTION

HOLOGRAPHIC multiple-input multiple-output (H-MIMO) communication is an emerging paradigm that extends conventional MIMO systems by integrating densely packed antennas on nearly continuous electromagnetically large surfaces [1], [2]. Unlike traditional MIMO systems, where antennas are treated as discrete elements, HMIMO envisions the transceiver as a nearly continuous aperture, capable of shaping, controlling, and sensing electromagnetic (EM) waves with extremely high spatial resolution. A key advantage of HMIMO lies in its ability to exploit the full aperture to generate highly directive beams, leading to improved energy focusing, improved spectral efficiency, better robustness in a multipath environment, and enabling radiative near-field communications by exploiting a large number of spatial degrees of freedom (DoF), even in line-of-sight (LoS) scenarios [3]. Orbital angular momentum (OAM), on the other hand, is an emerging concept in wireless communication systems that utilizes the helical phase structure of EM waves to multiplex multiple data streams on the same frequency and polarization channel, leveraging an additional spatial degree of freedom [4], [5].

In recent years, several research studies have explored the potential to utilize the OAM characteristic of EM waves to distinguish between different physical transmission paths or resources. The idea is that by using the unique spatial structure of the OAM modes, it could be possible to create a larger number of orthogonal communication channels, thus increasing the capacity of wireless communication systems [6]. The authors in [7] proposed a space division multiplexing technique that uses the orthogonality of communication modes for OAM transmission. In addition, an OAM-based mode division multiple access (OAM-MDMA) scheme has been introduced in [8] as a potential solution to accommodate a greater number of users. Similarly, the authors in [9] proposed a novel leakage-based capacity enhancement scheme for multi-user communications. However, many open challenges remain, as system performance has been shown to be highly dependent on various factors such as the type of antenna used, the overall architecture of the system, the operating frequency, and other implementation details [10]. Despite the initial enthusiasm surrounding OAM, several studies have pointed out that the OAM property of radio waves may not offer significant advantages over conventional MIMO techniques [11]. Recently, the authors in [12], introduced beam focusing for the HMIMO system that uses OAM employing large intelligent surfaces (LIS) for near-field LoS communications. Interestingly, the relationship between OAM-carrying EM waves and the communication modes is examined and shows that continuous phase shifters are sufficient to implement the precoder without requiring the channel state information. Similarly, [13] proposed polar Walsh functions to design communication modes that are orthogonal with constant amplitude. At the same time, the modes are separable in both radial and angular coordinates with slight performance degradation compared to the benchmark schemes. However, these works are limited to a single-polarized (SP) channel model for communications. Motivated by these works, this paper aims to analyze the performance of OAM-HMIMO while utilizing polarization multiplexing along with OAM by jointly exploiting orthogonal modes and multiple polarized channels.

Contributions – We theoretically evaluate the performance of OAM-HMIMO with multiple closely spaced uniform circular array (multi-UCA) apertures. We also utilize the EM information theory (EIT)-based channel model to enable polarization multiplexing in the OAM-HMIMO system. Furthermore, we demonstrate through a practical microstrip patch antenna array measurement that optimal OAM modes can be achieved through efficient design of the antenna array, while

---

This work is supported by the Electromagnetic Environment Hub (EME Hub), funded by Defence Science and Technology Laboratory (DSTL), UK.

979-8-3315-7896-1/26/$31.00 ©2026 IEEE

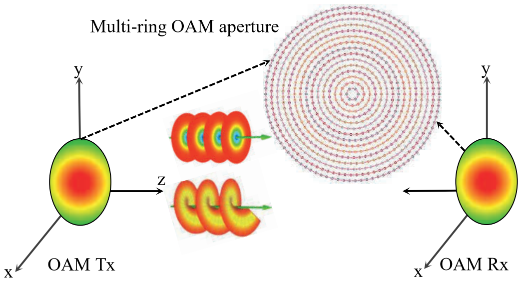

Fig. 1: HMIMO transceiver with multi-UCA-based OAM apertures.

the Green's function provides an accurate approximation of the field pattern generated by the OAM modes.

Organization –The rest of the paper is organized as follows. Section II presents a detailed HMIMO system and channel model. Section III presents the OAM model followed by the analytical capacity formulation in Section III-A. The performance evaluation based on the measured radiation response of a UCA, followed by extensive simulations of the theoretical framework, is presented in Section IV. Finally, Section V concludes the paper.

II. SYSTEM MODEL

We consider an HMIMO communication model, where the transmitter (Tx) and receiver (Rx) utilize a multiple UCA-based aperture for multiplexed OAM transmission, as shown in Fig. 1. The antenna elements on the Tx source and Rx apertures are uniformly distributed in k_υ, $\upsilon \in \{s, r\}$, numbers of rings each with circumference $|\mathcal{S}_{n_\upsilon}| = 2\pi R^2_{n_\upsilon}$ such that $\mathcal{S}_t = \{(x, y, 0) \in \mathbb{R}^3 : x^2 + y^2 = R^2_{k_t}\}$ and $\mathcal{S}_r = \{(x, y, \mathcal{D}^r_t) \in \mathbb{R}^3 : x^2 + y^2 = R^2_{k_r}\}$, where $\mathcal{D}^r_t$ denotes the separation distance and R_{k_υ} is the radius of the kth ring on the υth aperture. The number of antennas in the kth ring of the υth aperture is N_{k_υ} with constant inter-element spacing Λ_d. Furthermore, we assume that the antennas on the υth aperture are rectangular antennas (similar to a microstrip patch) each with a surface area $\Delta_\upsilon = \Delta_x \Delta_y$, where Δ_x and Δ_y denote the horizontal and vertical lengths of the patch, respectively, and are made from ideal metamaterial structures capable of independently tuning their reflection coefficients for all three polarization states. The phase configuration in the three polarizations is given by

$$\Phi_{n_s} = \text{diag}[E^{(x)}_{n_s} e^{i\theta^{(x)}_{n_s}}, E^{(y)}_{n_s} e^{i\theta^{(y)}_{n_s}}, E^{(z)}_{n_s} e^{i\theta^{(z)}_{n_s}}],$$

where $E^{(j)}_{n_t}$ and $\theta^{(j)}_{n_s} \in [0, 2\pi]$ are the amplitude and phase shift in the jth polarization, respectively, $j \in \{x, y, z\}$. The EM propagated in the z direction has an instantaneous electric field given by $\boldsymbol{E}(t) = E^{(x)}(t)\hat{x} + E^{(y)}(t)\hat{y} + E^{(z)}(t)\hat{z}$, where $E^{(j)}(t) = E^{(j)}_{n_t} e^{i\left(\omega t + \theta^{(j)}_{n_t}\right)}$ and ω is the angular frequency.

The radiated electric field, $\boldsymbol{E}(\boldsymbol{r})$, at an arbitrary point in the free space $\boldsymbol{r} = [r_x, r_y, r_z]$, excited by the current distribution $\boldsymbol{\mathcal{J}}(\boldsymbol{s}) \in \mathbb{R}^3$ at an arbitrary point $\boldsymbol{s} = [s_x, s_y, s_z]$ located at antenna element on the kth ring of the Tx aperture is a solution of the inhomogeneous Helmholtz equation $\boldsymbol{\nabla} \times \boldsymbol{\nabla} \times \boldsymbol{E}(\mathbf{r}) - \kappa_0^2 \boldsymbol{E}(\boldsymbol{r}) = i\kappa_0 \eta \boldsymbol{\mathcal{J}}(\boldsymbol{s})$, where $\boldsymbol{\nabla}$ is the gradient operator, $\eta = 120\pi$ is the intrinsic impedance and $\kappa_0 = 2\pi/\lambda$ denotes the wave number in free space [14]. The incurred electric field received at location $\boldsymbol{r}_m$ on the mth Rx antenna element, imposed by the current distribution at location $\boldsymbol{s}_n$ on the nth Tx antenna element, can be expressed as

$$\boldsymbol{E}_{\boldsymbol{r}_m} = \frac{\eta}{2\lambda} \int_{\mathcal{S}_r} \int_{\mathcal{S}_t} \boldsymbol{G}(\boldsymbol{r}_m, \boldsymbol{s}_n) \boldsymbol{\mathcal{J}}(\boldsymbol{s}_n) \mathrm{d}\boldsymbol{s}_n \mathrm{d}\boldsymbol{r}_m + \boldsymbol{\mathcal{N}}_{\boldsymbol{r}_m}, \quad (1)$$

where $\boldsymbol{\mathcal{N}}_{\boldsymbol{r}_m} = \mathcal{S}_r \boldsymbol{\mathcal{N}}$ denotes the uniformly distributed noise on the surface of the Rx antenna element and $\boldsymbol{G}(\boldsymbol{r}_m, \boldsymbol{s}_n) \in \mathbb{C}^{3\times 3}$ denotes the dyadic Green function given by

$$\boldsymbol{G}(\boldsymbol{r}_m, \boldsymbol{s}_n) = G_1(D_{mn}) \boldsymbol{I}_3 + G_2(D_{mn}) \boldsymbol{p}_{mn} \boldsymbol{p}^T_{mn}, \quad (2)$$

where D_{mn} denotes the distance between $\boldsymbol{r}_m \in \mathcal{S}_r$ and $\boldsymbol{s}_n \in \mathcal{S}_t$, $\boldsymbol{I}_3$ denotes the 3×3 identity matrix,

$$G_1(D_{mn}) = \frac{-i}{4\pi\kappa_0^2 D^3_{mn}} \left(-1 - i\kappa_0 D_{mn} + \kappa_0^2 D^2_{mn}\right) \tilde{g}(D_{mn}),$$

$$G_2(D_{mn}) = \frac{-i}{4\pi\kappa_0^2 D^3_{mn}} \left(3 + 3i\kappa_0 D_{mn} - \kappa_0^2 D^2_{mn}\right) \tilde{g}(D_{mn}),$$

$\tilde{g}(D_{mn}) = \exp(-i\kappa_0 D_{mn})$, and the term $\boldsymbol{p}_{mn}\boldsymbol{p}^T_{mn}$ in (2) defines the polarization direction between the pair of antennas and can be further expressed in fully polarized (FP) systems as follows:

$$\boldsymbol{p}_{mn}\boldsymbol{p}^T_{mn} = \begin{bmatrix} \cos x \cos x & \cos x \cos y & \cos x \cos z \\ \cos y \cos x & \cos y \cos y & \cos y \cos z \\ \cos z \cos x & \cos z \cos y & \cos z \cos z \end{bmatrix}, \quad (3)$$

where $\cos x = (r_x - s_x)/D_{mn}$, $\cos y = (r_y - s_y)/D_{mn}$, and $\cos z = (r_z - s_z)/D_{mn}$.

The channel gain between the (m, n)-th antenna pair located in the transceiver aperture is given by $\boldsymbol{\mathcal{G}}_{mn} = \frac{\eta}{2\lambda} \int_{\mathcal{S}_r} \int_{\mathcal{S}_t} \boldsymbol{G}(\boldsymbol{r}_m, \boldsymbol{s}_n) \mathrm{d}\boldsymbol{s}_n \mathrm{d}\boldsymbol{r}_m$. For perfectly aligned paraxial apertures, the electric field received at Rx can be expressed as

$$\boldsymbol{E} = \boldsymbol{\mathcal{G}} \boldsymbol{\mathcal{J}}_s + \boldsymbol{\mathcal{N}}, \quad (4)$$

where $\boldsymbol{E} = [\boldsymbol{E}_1, \boldsymbol{E}_2, \ldots, \boldsymbol{E}_{N_{k_r}}]^T$ is a $3N_{k_r} \times 1$ vector denoting the total electric field at the Rx aperture such that $\forall j \in \{1, 2, \ldots, N_{k_r}\}$, $\boldsymbol{E}_j = [E^{(x)}_j, E^{(y)}_j, E^{(z)}_j]$, $\boldsymbol{\mathcal{J}}_s = [\boldsymbol{\mathcal{J}}_1, \boldsymbol{\mathcal{J}}_2, \ldots, \boldsymbol{\mathcal{J}}_{N_{k_t}}]^T$ is a $3N_{k_t} \times 1$ current matrix such that $\boldsymbol{\mathcal{J}}_j = [\mathcal{J}^{(x)}_s, \mathcal{J}^{(y)}_s, \mathcal{J}^{(z)}_s]$, $\boldsymbol{\mathcal{N}} = [\mathcal{N}_1, \mathcal{N}_2, \ldots, \mathcal{N}_{k_r}]^T$ is the $3N_{k_r} \times 1$ noise vector, and $\boldsymbol{\mathcal{G}}$ is $3N_{k_r} \times 3N_{k_t}$ is the channel matrix. The channel gain between the (m, n)th Tx-Rx antenna pair can be approximated in closed-form expression following the procedure in [16], and is given by

$$\boldsymbol{\mathcal{G}}_{mn} = \frac{\Delta_t \Delta_r}{4\pi D_{mn}} \tilde{g}(D_{mn}) \,\text{sinc}\left(\frac{\kappa_0 (r_x - s_x) \Delta_x}{2D_{mn}}\right) \text{sinc}\left(\frac{\kappa_0 (r_y - s_y) \Delta_y}{2D_{mn}}\right) \boldsymbol{\zeta}_{mn}, \quad (5)$$

where $\Delta_t = \Delta_r$ denotes the area of the rectangular patch antenna in the corresponding aperture and $\boldsymbol{\zeta}_{mn}$ is given by

$$\boldsymbol{\zeta}_{mn} = \frac{-i}{4\pi\kappa_0^2 D_{mn}^3}\left(\left(-1 - i\kappa_0 D_{mn} + \kappa_0^2 D_{mn}^2\right)\boldsymbol{I}_3 + \left(3 + 3i\kappa_0 D_{mn} - \kappa_0^2 D_{mn}^2\right)\boldsymbol{p}_{mn}\boldsymbol{p}_{mn}^T\right). \quad (6)$$

The overall FP channel matrix can be expressed as

$$\boldsymbol{\mathcal{G}} = \begin{bmatrix} \boldsymbol{\mathcal{G}}^{(xx)} & \boldsymbol{\mathcal{G}}^{(xy)} & \boldsymbol{\mathcal{G}}^{(xz)} \\ \boldsymbol{\mathcal{G}}^{(yx)} & \boldsymbol{\mathcal{G}}^{(yy)} & \boldsymbol{\mathcal{G}}^{(yz)} \\ \boldsymbol{\mathcal{G}}^{(zx)} & \boldsymbol{\mathcal{G}}^{(zy)} & \boldsymbol{\mathcal{G}}^{(zz)} \end{bmatrix}, \quad (7)$$

where $\boldsymbol{\mathcal{G}}^{(pq)}$, $\forall p, q \in \{x, y, z\}$, is $N_{k_r} \times N_{k_t}$ matrix and the (m, n)th entry, $\mathcal{G}_{mn}^{(pq)}$, denotes the channel gain between the (m, n)th pair of antennas in polarization pq.

III. ORBITAL ANGULAR MOMENTUM

The OAM waves refer to the spatial structure of the EM field and its rotation around the central axis of the beam. A distinctive feature of EM waves carrying non-zero OAM is the emergence of continuous, helically shaped wavefronts that torqued around the direction of propagation. To fully characterize the EM field in terms of OAM, a complete vectorial analysis is typically required. However, even under the scalar field approximation, the helical nature of OAM wavefronts is commonly represented by an exponential phase factor of the form $\exp(jl\phi)$, where ϕ is the transverse azimuthal angle or phase and $l \in \mathbb{Z}$ denotes the topological charge which characterized each vortex or the OAM mode. The magnitude $|l|$ indicates the number of twists the wavefront completes over a unit wavelength distance, and the sign of l determines the direction of the twist. A notable property of OAM modes is their inherent orthogonality, which, in principle, allows spatial multiplexing by enabling multiple beams to co-exist without interference [12]. Let us assume that the pair of the (m, n)th antennas is located on the kth ring of Tx and Rx, the position vectors are characterized by $r_{k_t} = R_{k_t}(\hat{\boldsymbol{x}}\cos(\phi_{k_t}) + \hat{\boldsymbol{y}}\sin(\phi_{k_t}))$ and $r_{k_r} = R_{k_r}(\hat{\boldsymbol{x}}\cos(\phi_{k_r}) + \hat{\boldsymbol{y}}\sin(\phi_{k_r}))$, respectively. This distance separation between the antenna pair on the transceiver is written as

$$D_{mn} = \sqrt{R_{k_t}^2 + R_{kr}^2 + 2R_{k_t}R_{k_r}\cos\left(\phi_{kr} - \phi_{kt}\right) + \mathcal{D}_t^r}, \quad (8)$$

where $\mathcal{D}_t^r$ denotes the center separation between Tx and Rx. The channel matrix $\boldsymbol{\mathcal{G}}^{(pq)}$ for polarization pq given in (7) is a circulant matrix and can be diagonalized by the discrete Fourier transform (DFT) matrix $\boldsymbol{\mathcal{D}} = [\boldsymbol{d}_1, \boldsymbol{d}_2, \cdots, \boldsymbol{d}_L]$ of dimension $N_{k_t} \times L$, where L denotes the total number of OAM modes and $\boldsymbol{d}_l \in \mathbb{C}^{N_{k_t} \times 1}$ is an eigenvector of the DFT matrix corresponding to the lth OAM mode. For the lth unfocused OAM mode[1], $\boldsymbol{d}_l$ is given by [15]

$$\boldsymbol{d}_l = \frac{1}{\sqrt{N_{k_t}}}\exp\left(j\left(\frac{2\pi(\boldsymbol{N} - \boldsymbol{1})l}{N_{k_t}}\right)\right), \quad (9)$$

where $\boldsymbol{N}$ denotes the vector containing the index of the antenna elements, $\boldsymbol{1}$ is a column vector with all entries equal to 1 and l is the OAM mode.

The lth OAM mode is generated by

$$l = \begin{cases} -\frac{\tilde{n}-1}{2}, & \text{if } \tilde{n} \text{ is odd} \\ \frac{\tilde{n}}{2}, & \text{if } \tilde{n} \text{ is even} \end{cases}, \quad (10)$$

where $\tilde{n} = 1, 2, \cdots, L$, $\boldsymbol{l}$ is a vector that contains the OAM modes $0, +1, -1, +2, -2, \cdots, N_{n_k} - 1/2$.

In case of the conventional SP channel, with the electric field vector of the EM wave oscillates only in the x or y direction, while wave propagation is along the z direction, the channel gain in (7) can be diagonalized using a DFT matrix as follows.

$$\boldsymbol{\Lambda}^{(SP)} = \boldsymbol{\mathcal{D}}^H\boldsymbol{\mathcal{G}}^{(xx)}\boldsymbol{\mathcal{D}} = \begin{cases} \Lambda_{ij} \in \mathbb{C}, & \text{if } i = j \\ 0, & \text{if } i \neq j \end{cases}. \quad (11)$$

In case of FP systems, we assume that Tx has three perfectly orthogonal polarizations without cross-polarized channel gain. This can be achieved by employing the Gaussian elimination (GE) based precoding scheme in Tx by perfectly eliminating $\boldsymbol{\mathcal{G}}^{(pq)}$, $\forall p \neq q$, terms from the channel gain in (7) [16]. Then, the FP channel can be diagonalized using the DFT matrix as

$$\boldsymbol{\Lambda}^{(FP)} = \begin{bmatrix} \tilde{\boldsymbol{\Lambda}}^{(xx)} & \boldsymbol{0} & \boldsymbol{0} \\ \boldsymbol{0} & \tilde{\boldsymbol{\Lambda}}^{(yy)} & \boldsymbol{0} \\ \boldsymbol{0} & \boldsymbol{0} & \tilde{\boldsymbol{\Lambda}}^{(zz)} \end{bmatrix}, \quad (12)$$

where $\tilde{\boldsymbol{\Lambda}}^{(pq)} = (\boldsymbol{\mathcal{D}}^{(p)})^H\boldsymbol{\mathcal{G}}^{(pq)}\boldsymbol{\mathcal{D}}^{(p)}$, $\forall p = q$ and $p, q \in \{x, y, z\}$, is the diagonalized channel gain of the pq polarization state.

Using polarization multiplexing, Tx can send identical OAM modes on multiple orthogonal linear polarization independently, improving capacity without inter-channel interference among different polarizations.

A. Capacity Formulation

In this section, we evaluate the capacity expression for the diagonalized channel gain in the case of SP and FP while considering the single-ring and multiple-ring HMIMO OAM systems.

B. Single Ring Model with Closely Spaced Antennas

Assuming a single-ring model with diagonalized SP channel in (11), the capacity can be expressed as

$$C^{(SP)} = \log_2\left(\det\left(\boldsymbol{I} + \frac{P_t}{\sigma^2}\boldsymbol{\Lambda}^{(SP)}\boldsymbol{Q}\boldsymbol{\Lambda}^{(SP)^H}\right)\right), \quad (13)$$

where P_t denotes the total transmit power, σ^2 is the noise variance, and $\boldsymbol{Q}^{(pq)}$ is the $N_{k_t} \times N_{k_t}$ power allocation matrix such that $\text{Tr}(\boldsymbol{Q}^{(pq)}) \leq 1$.

Similarly, for FP systems with block diagonal channel matrix given in (12), the capacity can be expressed as the sum of

---

[1] In this work, we assume the case where the distance to the Rx is not known to the Tx, therefore, the unfocused OAM modes are generated by the OAM Tx.

the capacity over diagonalized channels in three independent polarizations, given by

$$C^{(FP)} = \sum_{\substack{p,q \\ p=q}} \log_2 \left(\det \left(\boldsymbol{I} + \frac{P_t}{\sigma^2} \tilde{\boldsymbol{\Lambda}}^{(pq)} \boldsymbol{Q}^{(pq)} (\tilde{\boldsymbol{\Lambda}}^{(pq)})^H \right) \right), \tag{14}$$

In case of a suboptimal power allocation scheme, the power is divided equally between the three perpendicular polarizations such that $\boldsymbol{Q}^{(pq)} = \boldsymbol{I}/(3N_{k_t})$, otherwise the capacity is maximized by employing the optimal power allocation strategy that can be adopted by assigning power to the individual channel in each polarization according to the waterfilling algorithm. From (14), it can be deduced that considering a uniform power allocation over each polarization and channels, the capacity can be at least doubled given that Rx is located close to Tx while assuming perfect polarization without mismatch.

C. UCA with Multiple Closely Spaced Rings

Consider a UCA-based aperture where the total antenna elements are arranged in multiple rings and the spacing between the antennas and rings is uniform throughout the aperture and is less than $\lambda/2$. The overall channel gain matrix can then be expressed as

$$\boldsymbol{\mathcal{G}}_{\text{OAM}} = \begin{bmatrix} \boldsymbol{\mathcal{G}}_{\text{OAM}_{11}} & \boldsymbol{\mathcal{G}}_{\text{OAM}_{12}} & \cdots & \boldsymbol{\mathcal{G}}_{\text{OAM}_{1k_t}} \\ \boldsymbol{\mathcal{G}}_{\text{OAM}_{21}} & \boldsymbol{\mathcal{G}}_{\text{OAM}_{22}} & \cdots & \boldsymbol{\mathcal{G}}_{\text{OAM}_{2k_t}} \\ \vdots & \vdots & \ddots & \vdots \\ \boldsymbol{\mathcal{G}}_{\text{OAM}_{k_r1}} & \boldsymbol{\mathcal{G}}_{\text{OAM}_{k_r2}} & \cdots & \boldsymbol{\mathcal{G}}_{\text{OAM}_{k_rk_t}} \end{bmatrix}, \tag{15}$$

where $\boldsymbol{\mathcal{G}}_{\text{OAM}_{ij}}$ denotes the channel gain between the ith UCA ring in Tx and the jth UCA ring in the Rx aperture. For FP systems, $\boldsymbol{\mathcal{G}}_{\text{OAM}_{ij}}$ is the equivalent channel gain in (7). Each polarized channel is diagonalized independently using the DFT, and the overall DFT matrix takes the form of

$$\boldsymbol{\mathcal{D}}_{\text{OAM}} = \begin{bmatrix} \boldsymbol{\mathcal{D}}_{\text{OAM}_1} & \boldsymbol{0} & \cdots & \boldsymbol{0} \\ \boldsymbol{0} & \boldsymbol{\mathcal{D}}_{\text{OAM}_2} & \cdots & \boldsymbol{0} \\ \vdots & \vdots & \ddots & \vdots \\ \boldsymbol{0} & \boldsymbol{0} & \cdots & \boldsymbol{\mathcal{D}}_{\text{OAM}_{k_t}} \end{bmatrix}, \tag{16}$$

where $\boldsymbol{\mathcal{D}}_{\text{OAM}_i}$ denotes a block diagonal DFT matrix for each polarized channel matrix of the ith ring. For OAM processing, the DFT matrix is applied to each polarized channel generated by the set of antenna elements located on each ring of the Tx such that $\boldsymbol{\Lambda}_{\text{OAM}}^{(FP)} = \boldsymbol{\mathcal{D}}_{\text{OAM}}^H \boldsymbol{\mathcal{G}}_{\text{OAM}} \boldsymbol{\mathcal{D}}_{\text{OAM}}$.

The capacity of the FP OAM-HMIMO transceiver with multiple-ring aperture can be expressed as

$$\begin{aligned} C_{\text{OAM}}^{(FP)} &= \log_2 \left(\det \left(\boldsymbol{I} + \frac{P_t}{\sigma^2} \boldsymbol{\Lambda}_{\text{OAM}}^{(FP)} \boldsymbol{Q}^{(pq)} \boldsymbol{\Lambda}_{\text{OAM}}^{(FP)^H} \right) \right) \\ &\overset{(a)}{=} \sum_i \sum_{\substack{p,q \\ p=q}} \log_2 \left(\det \left(\boldsymbol{I} + \frac{P_t}{\sigma^2} \tilde{\boldsymbol{\Lambda}}_{\text{OAM},i}^{(pq)} \boldsymbol{Q}^{(pq)} (\tilde{\boldsymbol{\Lambda}}_{\text{OAM},i}^{(pq)})^H \right) \right), \end{aligned} \tag{17}$$

where (a) follows the determinant of the block diagonal matrix $\boldsymbol{A}$ with the ith submatrix denoted by $\boldsymbol{a}_i$, that is, $\det(\boldsymbol{A}) = \prod_i \det(\boldsymbol{a}_i)$.

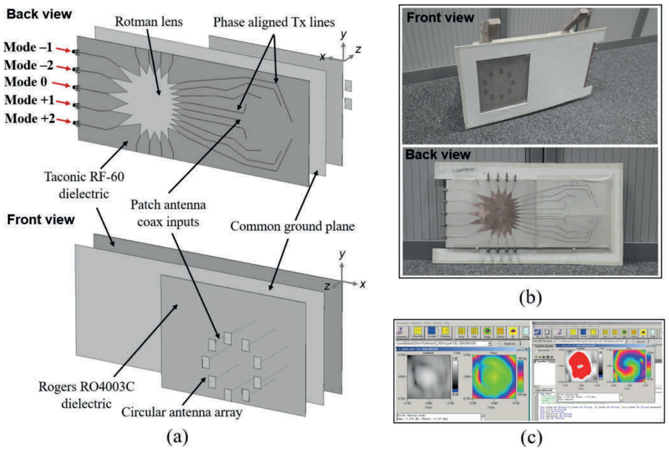

Fig. 2: Fabricated SP UCA: (a) front and back view of the array structure capable of generating 5 OAM modes, (b) fabricated array, and (c) NF scanning results from the NSI near-field Anechoic Chamber.

IV. RESULTS AND DISCUSSIONS

In this section, we first validate the theoretical performance of single-ring SP systems through measurements and then extend the analysis for multi-ring OAM-assisted FP HMIMO systems. The measurement-based magnitude and phase profiles for different OAM modes are compared with the one approximated by Green's function in (2).

A. Measurement Setup

To validate the theoretical approximation of the field generated by different OAM modes, we carried out practical experimentation on an in-house designed and fabricated UCA with $N_{k_t} = 9$, as shown in Fig. 2. The elements of the UCA antenna are uniformly distributed over a ring with an approximate diameter of 105 mm. Each unit cell of the UCA is vertically polarized and is implemented using microstrip patch antenna technology with dimensions of $20 \times 13.20\text{mm}^2$. The antenna is fed through a coaxial probe located 3.10mm from the broader edge. The UCA is designed to operate at a central frequency of 5.8 GHz manufactured on a Rogers RO4003C substrate with dimensions $274.00 \times 198.00 \times 0.51\text{mm}^3$ with a relative dielectric constant $\epsilon_r = 3.38$ and a tangent loss of $\tan\delta = 0.027$. To generate OAM modes, a Rotman lens built on a Taconic RF-60 substrate with dimensions of $477.00 \times 198.00 \times 0.64\text{mm}^3$ is used. A feed network on the same RF-60 substrate (dielectric constant of $\epsilon_r = 6.15$ and loss tangent of $\tan\delta = 0.0038$) is used to connect the UCA to the Rotman lens. The Rotman lens comprises 9 array ports and 5 beam ports to generate $L = 5$ distinct OAM modes such that $l = 0, \pm1, \pm2$, where each array port is connected to the antenna element on the UCA using phase-matched transmission lines to ensure accurate mode excitation [17]. The beam ports of the Rotman lens are used to ensure the orthogonality of the generated OAM modes. The field patterns

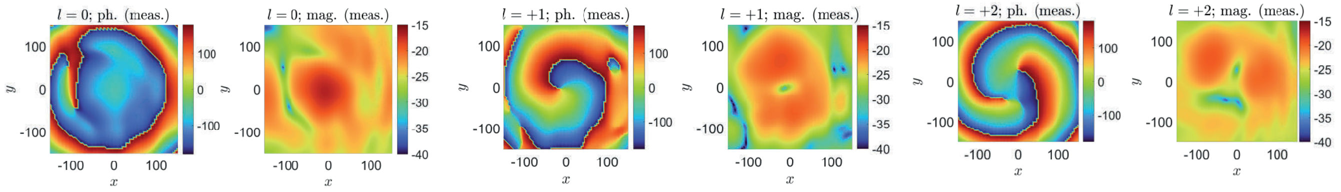

Fig. 3: Measurement based phase/magnitude profiles of SP (vertical-polarized) array for different OAM modes.

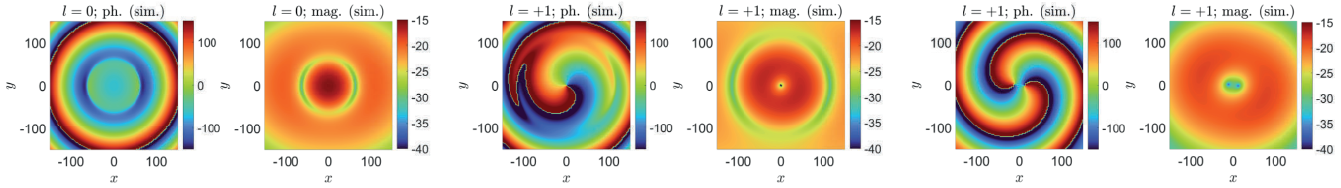

Fig. 4: Simulation based phase/magnitude profiles where the colorbars are in degrees (phase) and dB (magnitude).

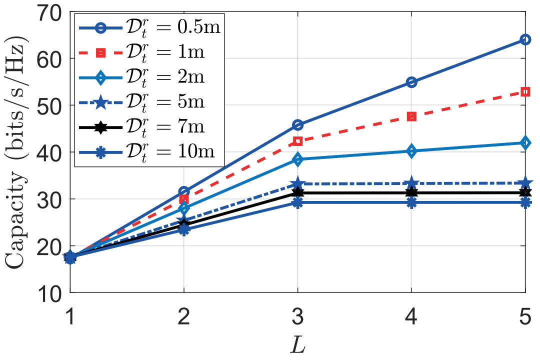

Fig. 5: Capacity performance of single ring UCA as a function of total number of OAM modes (L) and varying Tx-Rx separations ($\mathcal{D}_t^r$).

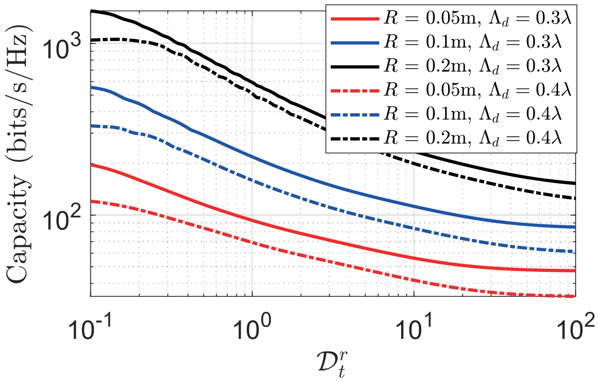

Fig. 6: Capacity performance of multiple ring UCAs as a function of Tx and Rx aperture size (R) and the spacing between antennas (Λ_d).

for particular OAM modes are scanned in a near-field system-incorporated (NSI) anechoic chamber.

Fig. 3 shows the magnitude and phase profile of the measured field pattern for the three corresponding OAM modes with $l = 0, +1, +2$ while similar agreement is observed for modes -1 and -2 and are skipped here. Taking into account the same operating setup, the phase and magnitude profiles of the field patterns approximated by the Green's function are provided in Fig. 4 for comparison. It is evident from the qualitative comparison that the simulation results are in good agreement with the measurements, demonstrating reliable consistency between experimental validation and theoretical approximations used in the proposed approach.

B. Simulations Setup

Through extensive simulations, we evaluated the capacity of OAM-aided MIMO systems where the channel between Tx and Rx is modeled according to (5) for single-ring and multiple-ring scenarios. The operating frequency of the system is 5.8 GHz, $\sigma^2 = 5.6 \times 10^{-6}$, the transmit power is $P_t = 10$ dBm, and the maximum aperture is $R = R_t = R_r$. Unless stated otherwise, the same configuration is used as in Section IV-A.

Fig. 5 presents the theoretical capacity of a single-ring model presented in Section IV-A as a function of the OAM modes and the varying distance between Tx and Rx. It can be seen in the figure that increasing the number of OAM modes leads to improved capacity; however, a higher number of modes is more beneficial in a case where Rx is located in the near-field of Tx. The near field boundary is calculated by $2\left(2R_t + 2R_r\right)^2/\lambda \approx 1.5876$m where R_t and R_r denote the maximum radius of the aperture of Tx and Rx, respectively [18]. However, in the far field, an increase in the number of modes beyond 3 shows a negligible performance gain.

Fig. 6 shows the capacity as a function of the Tx-Rx

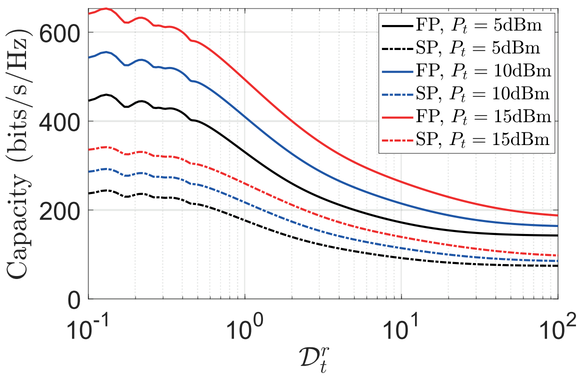

Fig. 7: Capacity performance of OAM-HMIMO with FP and SP multiple ring UCA aperture for a varying transmit power.

separation for different aperture sizes and antenna spacing in the case of multiple UCA-based apertures. In the simulation setup, the number of rings, with a uniform spacing of 0.3λ between the rings, is set to 3, 6, and 12 in the aperture of size $0.05, 0.1$, and 0.2m, respectively. Similarly, for the 0.4λ spacing, 2, 4, and 9 rings are accommodated in the fixed-size aperture. Furthermore, the maximum number of OAM modes utilized in each ring is set to $L = N_{k_t}/2$ such that $l = [0, +1, -1, +2, -2, \cdots, N_{k_t} - 1/2]$. Fig. 6 shows that the capacity decreases with distance, which is consistent with the observations made in Fig. 5. Furthermore, a large antenna spacing leads to performance degradation because a larger spacing results in accommodating fewer antennas in fixed aperture. Additionally, for fixed antenna spacing, a higher number of UCA rings can be placed on an aperture of a larger radius, which leads to higher capacity.

Fig. 7 presents the capacity performance of the FP OAM-HMIMO compared to the SP OAM-HMIMO for varying transmit power. In the simulation setup, we consider $\Lambda_d = 0.3\lambda$, aperture radius of 0.1m with 6 number of UCA rings and $L = 5$ such that $l = 0, \pm 1, \pm 2$. It is clear from the figure that the capacity performance of HMIMO can be further improved by utilizing polarization multiplexing together with OAM. The FP system in conjunction with OAM provides a higher capacity (solid lines) than the conventional SP counterpart (dotted lines). The reason behind the capacity improvement is that FP systems utilize multiple independent and orthogonal polarization to transmit different OAM modes. In addition, the increase in the transmit power at the Tx leads to better performance in the case where Rx is close enough to Tx with a separation distance less than 20m, while the performance improvement decreases as the Rx are located beyond this distance range.

V. Conclusion

In this paper, we have analyzed the performance of HMIMO by exploiting OAM and polarization multiplexing. The Green's function-based EM informed channel model was used to capture multiple polarizations in the considered system model. Theoretical analyses were performed for single- and multiple-ring UCAs. Through simulation results, it was demonstrated that utilization of the polarization multiplexing by transmitting orthogonal OAM modes over multiple independent polarizations improves the performance of the HMIMO systems. Moreover, the measurements obtained from the fabricated single-ring array validated the approximated OAM field patterns. In future work, our aim is to investigate more comprehensive system models adopting continuous apertures while considering practical design parameters and the impact of cross-polarization ratio and misalignment of OAM modes.

References

[1] T. Gong, et al., “Holographic MIMO communications: Theoretical foundations, enabling technologies, and future directions," *in IEEE Commun. Surveys & Tuts.*, vol. 26, no. 1, pp. 196 - 257, First Quart., 2024.

[2] O. Yurduseven, and D. R. Smith, “Dual-polarization printed holographic multibeam metasurface antenna, *IEEE Ant. and Wireless Prop. Lets.,* vol. 16, pp. 2738-2741, 2017.

[3] A. A. DAmico and L. Sanguinetti, “Holographic MIMO communications: What is the benefit of closely spaced antennas?." *IEEE Trans. on Wireless Commun.,* vol. 23, no. 10, pp. 13826-13840, 2024.

[4] Y. Zheng, S. Wang, X. Chu, W. Zheng, Z. Hu and Z. Lu, “A UCA-based orbital angular momentum solution for integrated sensing and communication systems," *in IEEE Wireless Commun. and Net. Conf. (WCNC),* Milan, Italy, 2025, pp. 1-6.

[5] Yurduseven, O., Marks, D.L., Gollub, J.N. and Smith, D.R., “Design and analysis of a reconfigurable holographic metasurface aperture for dynamic focusing in the Fresnel zone," *IEEE Access,* vol. 5, pp. 15055-15065, 2017.

[6] O. Edfors and A. J. Johansson, “Is orbital angular momentum (OAM) based radio communication an unexploited area? *IEEE Trans. on Ant. Prop.,* vol. 60, no. 2, pp. 1126–1131, 2012.

[7] J. Wang et al., “Terabit free-space data transmission employing orbital angular momentum multiplexing, *Nature Photonics,* vol. 6, no. 7, pp. 488496, 2012.

[8] W. Cheng, W. Zhang, H. Jing, S. Gao, and H. Zhang, “Orbital angular momentum for wireless communications, *IEEE Wireless Commun.,* vol. 26, no. 1, pp. 100-107, 2019.

[9] A. Yadanar Win, M. Berhane Teklu and Y. Ho Chung, “Novel leakage-based capacity enhancement scheme for multi-user OAM communications," *in IEEE Access,* vol. 13, pp. 67748-67757, 2025.

[10] R. Chen, et al., “Orbital angular momentum waves: Generation, detection, and emerging applications, *IEEE Commun. Surveys & Tuts.,* vol. 22, no. 2, pp. 840868, Second Quart., 2020.

[11] R. Gaffoglio, et al., “Vortex waves and channel capacity: Hopes and reality, *IEEE Access,* vol. 6, pp. 1981419822, 2017.

[12] G. Torcolacci, N. Decarli and D. Dardari, "OAM-based holographic MIMO using large intelligent surfaces," *in 2022 IEEE Global Commun. Conf. (GLOBECOM),* Rio de Janeiro, Brazil, 2022, pp. 651-655.

[13] C. Vanwynsberghe, J. He, C. Huang and M. Debbah, “Walsh meets OAM in holographic MIMO," *in 2023 Int. Conf. on Electromag. in Advanced App. (ICEAA),* Venice, Italy, 2023, pp. 593-596.

[14] Z. Wan, J. Zhu, Z. Zhang, L. Dai and C. -B. Chae, “Mutual information for electromagnetic information theory based on random fields," *in IEEE Trans. on Commun.*, vol. 71, no. 4, pp. 1982-1996, 2023.

[15] H. Sasaki, Y. Yagi, H. Fukumoto and D. Lee, “OAM-MIMO multiplexing transmission system for high-capacity wireless communications on millimeter-wave band," *in IEEE Trans. on Wireless Commun.*, vol. 23, no. 5, pp. 3990-4003, 2024.

[16] Wei, L., et al.,“Tri-Polarized holographic MIMO surfaces for near-field communications: Channel modeling and precoding design," *in IEEE Trans. on Wireless Commun.,* vol. 22, no. 12, pp. 8828-8842, 2023.

[17] A. Almradi, M. A. B. Abbasi, M. Matthaiou and V. F. Fusco, “On the spectral efficiency of orbital angular momentum with mode offset," *in IEEE Trans. on Veh. Tech.,* vol. 70, no. 11, pp. 11748-11760, 2021.

[18] S. Zeng, et al., “Revisiting near-far field boundary in dual-polarized XL-MIMO systems," *in IEEE Trans. on Wireless Commun.*, early access 2025. doi: 10.1109/TWC.2025.3559510.